



Refined room-temperature equation of state of Bi up to 260 GPa

Daniel J. Campbell , Daniel T. Sneed, E. F. O'Bannon, III, Per Söderlind, and Zsolt Jenei 
Lawrence Livermore National Laboratory, 7000 East Avenue, Livermore, California 94550, USA



(Received 17 March 2023; accepted 31 May 2023; published 15 June 2023)

At room temperature, bismuth undergoes several structural transitions with increasing pressure before taking on a body-centered cubic (bcc) phase at approximately 8 GPa. The bcc structure is stable to the highest measured pressure and its simplicity, along with its high compressibility and atomic number, makes it an enticing choice as a pressure calibrant. We present three data sets on the compression of bismuth in a diamond anvil cell in a neon pressure medium, up to a maximum pressure of about 260 GPa. The use of a soft pressure medium reduces deviatoric stress when compared to previous work. With an expanded pressure range, a higher point density, and a decreased uniaxial stress component, we are able to provide more reliable equation of state parameters. We also conduct density functional theory electronic-structure calculations that confirm that the bcc phase is energetically favored at high pressure.

DOI: [10.1103/PhysRevB.107.224104](https://doi.org/10.1103/PhysRevB.107.224104)

I. INTRODUCTION

Elemental bismuth has been the subject of extensive investigation at high pressure. At ambient temperature, it has a series of structural transitions under 10 GPa, passing through four different phases. Bi-I is rhombohedral and present up to about 2.5 GPa [1–3]. Bi-II is monoclinic and stable over less than 0.5 GPa. Bi-III is a complex host-guest phase [1–3]. Bi-IV is only observed above 150 °C, over approximately the same range as Bi-III. The final ambient temperature structure, body-centered cubic (bcc) Bi-V, emerges at around 8 GPa and has been shown to be stable through at least 200 GPa [4]. Dynamic compression work has shown that these phase boundaries are not necessarily fixed. The II and III phases may not appear in shock compression experiments [5–7] and other solid-solid or solid-liquid boundaries can move as much as several GPa depending on the compression rate [3,8].

Despite the complexity of the lower-pressure phase diagram, the stability of bcc Bi-V to high pressure is unquestioned. This simple structure is one reason why Bi has been an enticing choice for a pressure calibrant for experiments surpassing 100 GPa. Bi also has the highest atomic number of any nonradioactive element, resulting in a strong x-ray diffraction (XRD) signal. In addition to that, it is softer than many of the other materials (Au, Cu, Pt, NaCl) whose lattice parameters are used for determining pressure in XRD experiments. This means that the volume change with pressure is larger. This increases the precision of pressure determination, which is especially important at ultrahigh compression where the pressure-volume curve flattens out.

Despite the many reports on the structural transitions of Bi, only a limited number have extended far into the bcc phase. The highest pressure work, which reached 220 GPa, did not use a pressure-transmitting medium (PTM), counting on Bi itself to redistribute anisotropic stress [4]. We have carried out x-ray diffraction experiments on bismuth at ambient temperature up to 260 GPa, using neon as a soft pressure medium. With both Cu and Ne as reference pressure calibrants, we find

good agreement among three independent data sets. Differences in measured Bi volume at high pressure from previous reports are evidence that a soft pressure medium is necessary to minimize the uniaxial stress on the sample. In this way we are able to provide a more accurate Bi equation of state (EOS), extended to higher pressure. We also show the importance of a soft PTM in deriving accurate EOS values. The data presented in this paper will enable Bi to be used for precise pressure calibration at high pressures.

II. METHODS

Experiments were carried out at Sector 16 of the Advanced Photon Source, as part of the High-Pressure Collaborative Access Team (HPCAT), on three different samples loaded in diamond anvil cells (DACs). A set each of 200- μm flat and 100- μm /300- μm beveled culet anvils were used for experiments at station 16-BMD with 25-keV x rays, and 50- μm /300- μm beveled culets at 16-IDB with 30-keV x rays. We refer to the different experiments as runs A, B, and C, in decreasing order of culet size. Gaskets were indented to thicknesses of about 25 μm (A and B) and 20 μm (C), and holes were drilled in the center of the gaskets with diameters of 120, 55, and 20 μm for A, B, and C, respectively. The investigated samples were 5- μm -thick pieces of Bi foil (Goodfellow, 99.97%) cut to an appropriate size and placed in the gasket hole normal to the incoming x rays. The 200- μm culet DAC also contained copper foil (Goodfellow, 99.97%, 5 μm in thickness) and ruby for pressure calibration, while the 100- μm DAC contained a copper sphere approximately 10 μm in diameter. Neon gas served as the pressure medium in all cases and was introduced into the gasket hole with a high-pressure gas loader. The maximum pressure reached in each experiment was, in order, 89, 184, and 259 GPa. Pressure was increased during experiments via a helium gas membrane attached to the DAC. High-quality x-ray diffraction patterns, with good signal-to-noise ratio, were collected up to the highest pressures, as demonstrated in Fig. 1, which shows the 2D

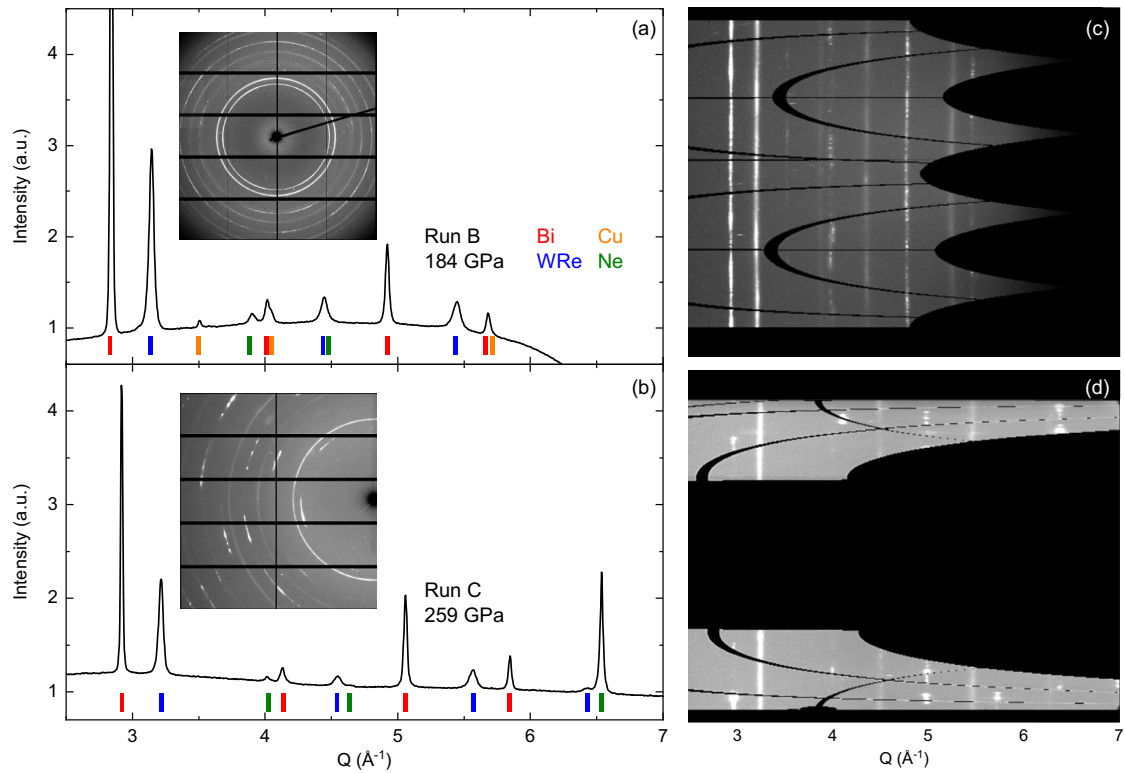


FIG. 1. The intensity as a function of Q at (a) 184 and (b) 259 GPa for runs B and C, respectively. These represent the highest pressures reached in each experiment. Ticks below the data mark the peaks for each material present (B had a Cu pressure marker, and C did not). The insets show the original two-dimensional detector images. Panels (c) and (d) are the corresponding cake images, created by unrolling the detector image to present it as a function of Q with the azimuthal angle along the y axis.

detector image, the caked diffraction image, and the intensity as a function of Q for the highest pressure points of Runs B and C. The detector configuration was the same in Runs A and B but different in Run C, where it covered less Q than in the other measurements.

Several crystal structures were considered in our theoretical modeling of Bi, namely, Bi-I (rhombohedral), Bi-II (monoclinic), simple cubic (sc), hexagonal close-packed (hcp), face-centered cubic (fcc), and finally the Bi-V structure (bcc). Structural relaxation was performed for the Bi-I and Bi-II phases, and the hcp phase was calculated with both an ideal c/a axial ratio (1.633) and an optimized (relaxed) axial ratio. Because we are primarily focused in this report on the high-pressure behavior, we do not consider the low-pressure Bi-III phase, which has a complex host-guest structure [1]. We apply DFT with the generalized gradient approximation (GGA) for the electron exchange and correlation functional. The methodology is implemented in an all-electron code to avoid the commonly used pseudopotential approximation that is often assumed in DFT calculations but tends to cause inaccuracies at very high compression. Specifically, we employ a full-potential linear muffin-tin orbital (FPLMTO) method [9] that has been shown to be very accurate for high-pressure studies for many materials including bismuth up to 100 GPa [10].

The FPLMTO technique does not make any approximations beyond that of the GGA and limitations of the basis set. Basis functions, electron densities, and potentials are

calculated without any geometrical approximation and these are expanded in spherical harmonics inside non-overlapping (muffin-tin) spheres surrounding each atom and in Fourier series in the region between these muffin-tin spheres. There is a choice in how to define the muffin-tin sphere radius; here it is chosen as 0.74 of the radius of a sphere with a volume equal to the atomic volume (Wigner-Seitz radius). The radial parts of the basis functions inside the muffin-tin spheres are calculated from a wave equation for the $l = 0$ component of the potential that includes all relativistic corrections including spin-orbit coupling for d and f states but not for the p states, following the comprehensive discussions of the spin-orbit interaction in Refs. [11,12]. All calculations utilize semicore states and valence states with two fixed-energy parameters each for the s semicore state, the p semicore state, and the valence states. There are six tail energies ranging from -3 to -0.2 Ry. Furthermore, we define 14 basis functions with $5s$, $5p$, and $4f$ semicore states in addition to the $6s$, $6p$, $5d$, and $5f$ valence states. The number of k -points included in the electronic-structure calculations depends on the particular crystal structure but we generally use about 1000 k -points or more for one atom/cell calculations and less for cells with many atoms. Each energy eigenvalue is broadened with a Gaussian having a width of 20 mRy. Total energies for each phase were calculated on a dense volume mesh of about 0.3 \AA^3 . The phonon dispersions for bcc Bi at about 21 GPa were calculated using the small displacement method [13] and a 27-atom supercell. The atomic forces required for the

phonons were extracted from the electronic structure total energies as previously described [14]. The resulting phonons showed no indications of any instability.

III. PRESSURE-VOLUME RELATION

At ambient temperature, Bi-I transitions to Bi-II, Bi-III, and finally Bi-V, while Bi-IV appears only above room temperature [2]. We saw evidence for all four ambient temperature structures during the initial pressure increase, with some coexistence of Bi-III and Bi-V past the latter's first appearance at around 8 GPa. Above 10 GPa in all runs, only Bi-V was observed in the pattern, and so all Bi-V data used for analysis start at 10 GPa. For Runs A and B the position of the Cu [111] reflection was used to calculate pressure [16]. For Run C pressure was determined using the Ne [111] peak. Our Ne EOS was calculated using the results of the 100- μm culet experiment, by calibrating the lattice parameter as determined by the Ne [111] reflection to the pressure as determined by Cu. Using a Vinet EOS form,

$$P = 3K_0 \left(\frac{1 - (V/V_0)^{1/3}}{(V/V_0)^{2/3}} \right) e^{\frac{3}{2}(K'_0 - 1)(1 - (V/V_0)^{1/3})}, \quad (1)$$

and fixing the ambient pressure atomic volume of Ne $V_0 = 22.234 \text{ \AA}^3$ as in Ref. [17], we obtain a bulk modulus $K_0 = 1.046 \pm 0.030 \text{ GPa}$ and its pressure derivative $K'_0 = 8.38 \pm 0.05$. The process of calibrating Ne to our own Cu data minimizes the uncertainty that could be introduced by using multiple pressure markers with separately determined equations of state. This method ensures that the pressure values in our data derive from the same source with the fewest intermediate steps possible. While they are independent of each other, preparation for Runs B and C was very similar. Our calibration also extends to 184 GPa, while some other commonly used Ne equations of state have only been determined up to around 100 GPa [18]. Our EOS parameters are very similar to the parameters determined by Dewaele *et al.* [17] up to 209 GPa, ($K_0 = 1.070 \pm 0.016 \text{ GPa}$ and $K'_0 = 8.40 \pm 0.03$, with the same $V_0 = 22.234 \text{ \AA}^3$ in both cases) (Ref. [19], Table S-II). However, as shown in the Supplemental Material (Ref. [19], Fig. S1), even the slight difference between the two leads to a 10-GPa difference at the maximum pressure and a clear difference in curvature when comparing multiple data sets.

Figure 2(a) shows the volume of Bi as a function of pressure for all three of our data sets, starting at 10 GPa when we observe only the bcc phase. The extracted lattice parameters for Bi-V, Cu, and Ne for all runs are available in the Supplemental Material (Ref. [19], Table S-III). Maximum pressures reached were 89, 184, and 259 GPa for the 200-, 100/300-, and 50/300- μm culet cells, respectively. For Run C, few data points were obtained below 100 GPa. Figure 2(b) shows a comparison to the previous data [4,15]. For the experiments of Ref. [4] no PTM was used, with only Bi foil and Pt (the pressure calibrant) in the cell. We would expect this to result in more anisotropic stress than in experiments with Ne as the PTM. While Ne solidifies above 4 GPa at ambient pressure, it is still much more compressible than Bi. Indeed, the upward deviation of the data of Ref. [4] at high pressure, clearest in the inset to Fig. 2(b), is what would be expected under less

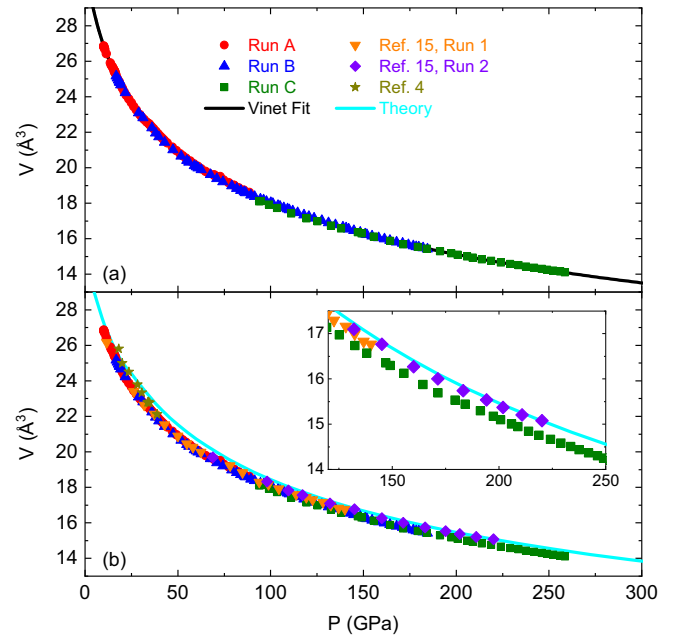


FIG. 2. (a) Pressure-volume relationship for Bi-V obtained from our three experiments, with 200- μm (red circles), 100- μm /300- μm (blue triangles), and 50- μm /300- μm (green squares) culets. The solid line is a fit to all three data sets using the Vinet equation of state with $K_0 = 38.2 \text{ GPa}$, $K'_0 = 5.8$, and $V_0 = 31.67 \text{ \AA}^3$. (b) The same data in panel (a) compared to data from Refs. [4,15] and our own theoretical calculations (solid line). The lower volume for a given pressure in our data is what would be expected for reduced deviatoric stress. The inset shows the highest-pressure region for Run C, the two runs of Ref. [4], and the calculated results.

hydrostatic conditions. Our three data sets also combine to give a much higher point density over the covered range.

We fit an EOS of the form given in Eq. (1) to extract K_0 , K'_0 , and V_0 . One issue with Bi is that, since the bcc structure is not stable at ambient pressure, the V_0 of Bi-V is not known, and small variations dramatically change the corresponding K_0 and K'_0 . We calculated the bulk modulus and its derivative for two different V_0 values: 32.23 and 31.67 \AA^3 . The theoretical ambient pressure volume of bcc Bi stemming from our calculations is 32.23 \AA^3 . The value of 31.67 \AA^3 is the result of letting all parameters of the fit vary. Notably, this value is quite similar to the volume obtained by accounting for the lattice collapse at each phase transition. The I-II, II-III, and III-V transitions produce volume collapses of 5.2%, 3.6%, and 2.3%, respectively, for a total of 10.7% volume decrease as a result of structural transitions alone [3]. Applied to the Bi-I ambient pressure volume of 35.46 \AA^3 , that gives us a value of 31.7 \AA^3 for Bi-V. Table I shows the K_0 and K'_0 obtained using fits with each volume and a fit to the calculated data, as well as values from other works. The theoretical values in Table I were obtained by a Vinet EOS fit to the calculated data points. In comparing two fits to the same experimental data, we find that while the choice of V_0 significantly changes K_0 and K'_0 , it has less impact on the actual pressure-volume curves. In Fig. 2(a) we use the values for $V_0 = 31.67 \text{ \AA}^3$, but Fig. 3(a) shows that the two curves are nearly indistinguishable over much of the range, as the changes in the bulk modulus and

TABLE I. Vinet equation of state parameters extracted from fits of all Bi data sets and our theoretical results. For fits stemming from this work, the data points from all three runs above 10 GPa were used. Uncertainty values are those obtained from the fit. V_0 was fixed to the value obtained via the theoretical calculation value for one of the fits, marked by an asterisk. Reference [15] provides several sets of EOS parameters from different experiments; we list those done in Ar, which extended to highest pressure.

K_0 (GPa)	K'_0	V_0 (\AA^3)	P_{max} (GPa)	Ref.
38.2 ± 1.5	5.8 ± 0.06	31.67 ± 0.19	259	Exp.
34.0 ± 0.2	6.0 ± 0.02	32.23*	259	Exp.
36.8 ± 1.0	6.0 ± 0.03	32.23 ± 0.13	462	Th.
35.22	6.303	31.60	222	[4]
42.7	5.3	—	52	[15]

the derivative are compensated by the change in the starting volume. The difference between the two only exceeds 1 GPa below 10 GPa, a pressure range where the Bi-V phase cannot be isolated [Fig. 3(b)]. Meanwhile, comparison to previous

work shows much more substantial spread, with a difference of more than 15 GPa from the EOS of Ref. [4] by the maximum pressure reached in that study (220 GPa).

IV. THEORETICAL RESULTS

Density functional theory calculations for the atomic volume of Bi-V at various pressures are shown in Fig. 2. In addition to that, we performed calculations of the energy difference between the bcc Bi-V structure and several other candidates: Rhombohedral (Bi-I), monoclinic (Bi-II), fcc, sc, and hcp with either an ideal or relaxed c/a axial ratio. Energies for the Bi-III structure were not calculated because of the complicated nature of the Bi-III host-guest structure and the fact that this work is mainly focused on higher pressures. We present the results as enthalpy ($H = E + PV$) differences of the various structures relative to the bcc (Bi-V) phase as functions of pressure.

While our focus in this work is on the pressure range where the bcc phase is clearly favorable, we will comment briefly on the low-pressure region where there is more competition [Fig. 4(b)]. The DFT model reproduces the correct ambient-pressure Bi-I phase and the pressure-induced transition to Bi-II. Experimentally, the transition takes place at around 2.5 GPa [3] while our calculations indicate a transition below 1 GPa. The relatively small discrepancy is not unusual for a first-principles approach and could be due to uncertainty in the DFT (e.g., the electron exchange or correlation functional) or the fact that the calculations assume zero temperature. A transition from Bi-II to Bi-V is predicted to occur at about 2.7 GPa. This is less relevant as we did not consider the Bi-III phase, though the experimental II-III transition does occur at a similar pressure. Far beyond 100 GPa, bcc is at far lower enthalpy over the two hcp phases, the next closest in energy, and the difference increases with pressure. Interestingly, the pressure behavior of fcc is rather similar to bcc but at an appreciably higher energy.

V. EVALUATION OF NONHYDROSTATIC STRESS

It is possible to quantify the amount of uniaxial stress on the sample via the shift in d spacing for different values of the Miller indices h , k , and l . Extensive discussion and analysis of this lineshift has been performed in other works [4,20–22]. For a cubic system, the basic equation for the nonhydrostatic lattice parameter from a specific hkl combination, a_m , is

$$a_m(h, k, l) = M_0 + M_1[3\Gamma(1 - 3\sin^2\theta)], \quad (2)$$

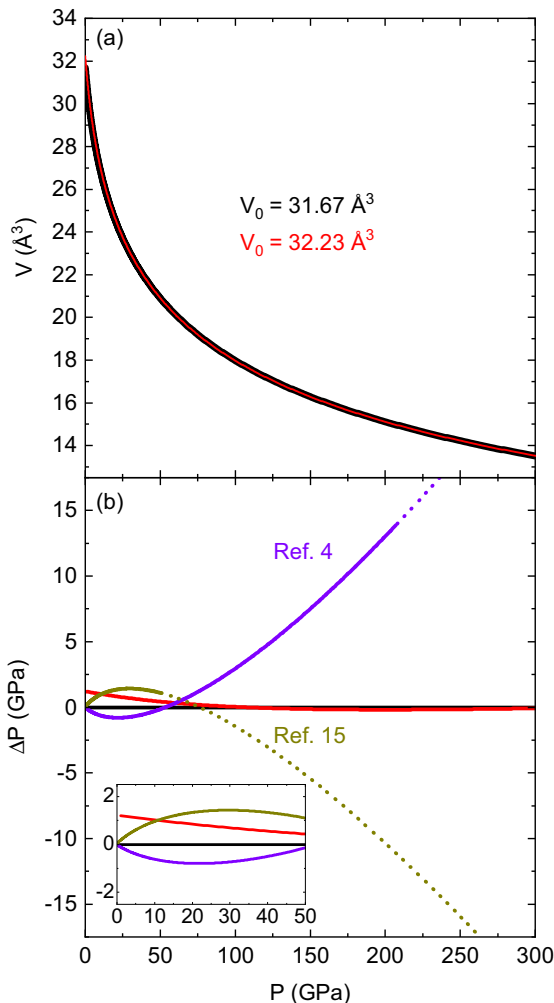


FIG. 3. (a) The P - V relation for Bi-V from Vinet equation of state fits to the data in Fig. 2 using two different ambient pressure volumes. Lines are different thicknesses as the data nearly completely overlap above 10 GPa. (b) The deviation from the fit with $V_0 = 31.67 \text{ \AA}^3$, for the other choice of V_0 and literature values. The latter transition from solid to dotted lines above the maximum pressure reached in the experiment. The inset shows a closeup of the 0–50 GPa range.

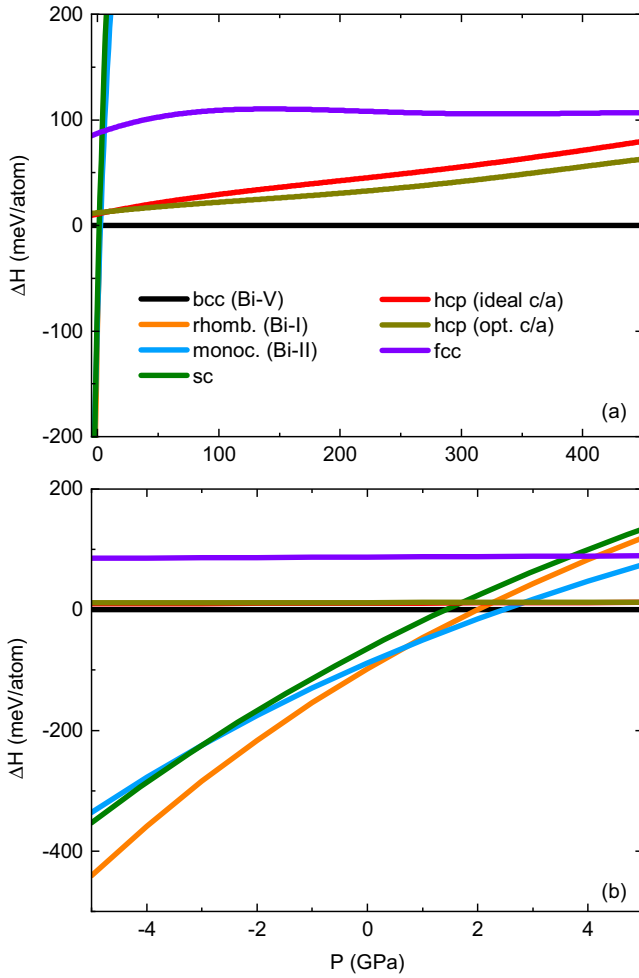


FIG. 4. Calculated enthalpy differences of various potential structures of bismuth relative to bcc Bi-V (the solid line at $\Delta H = 0$) as functions of pressure. Panel (a) shows the entire pressure range over which calculations were performed. The bcc structure is clearly favored after only a slight increase in pressure. Panel (b) shows a closeup of the low-pressure region. The first pressure-induced phase (Bi-II) becomes favored over the ambient ground-state (Bi-I) phase below 1 GPa. The Bi-III phase is not calculated (see Methods).

with

$$M_0 = a_P \{ [1 + (\alpha t/3)(1 - 3\sin^2\theta) \times (S_{11} - S_{12}) - (1 - \alpha^{-1})(2G_V)^{-1}] \} \quad (3)$$

$$M_1 = -a_P(\alpha S t/3) \quad (4)$$

$$\Gamma(h, k, l) = (h^2k^2 + k^2l^2 + h^2l^2)/(h^2 + k^2 + l^2)^2, \quad (5)$$

where a_P is the hydrostatic lattice parameter, S_{ij} are the components of the compliance tensor, $S = S_{11} - S_{12} - S_{44}/2$, and G_V is the shear modulus of randomly oriented polycrystals under isostrain conditions. t is the quantity of interest, and represents $\sigma_3 - \sigma_1$, the difference between the radial and axial stress components. To simplify things, we can approximate $M_0 \simeq a_P$, meaning that at each pressure a_m will be a linear function of $3(1 - 3\sin^2\theta)\Gamma$, with both θ and Γ functions only of h, k , and l . Therefore, a linear fit of a_m vs $3(1 - 3\sin^2\theta)\Gamma$ gives us M_0 and M_1 , and from Eq. (4) we can solve for

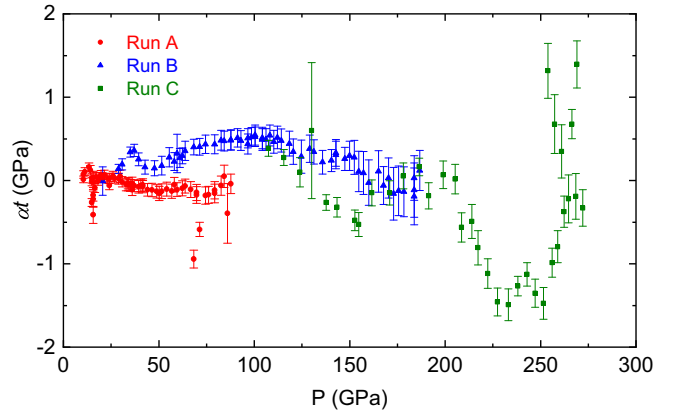


FIG. 5. Values of αt of Bi, assumed to be the material strength, for all three experiments, using lineshift analysis as described in the text. Error values are derived from the uncertainty of the d spacing from the peak-fitting program.

$\alpha t = -3 \frac{M_1}{M_0} \frac{1}{S}$. α determines the weighting of the shear moduli and takes on values ranging between 1 (for stress continuity) and 0.5 (halfway between stress and strain continuities). Since we cannot determine its value from our data, we present the combined product αt of our three data sets [Fig. 5].

Calculating αt requires values of the compliance tensor at each pressure point. Since these have not been measured experimentally up to such high pressures, we fit the theoretical results of Ref. [23] for the elastic tensor C_{ij} up to 191 GPa to a power law of the form $C_{ij}(P) = C_{ij}(0) + aP^n$, with $n \simeq 0.9$ for each of C_{11} , C_{12} , and C_{44} . These values were then extrapolated up to 259 GPa and converted to the necessary compliance tensor results via $S_{ij} = C_{ij}^{-1}$.

Our three data sets are shown in Fig. 5, where for each run the [110], [200], and [211] peak positions of Bi-V were used to calculate αt at each pressure. Error bars were estimated from the uncertainty of the initial fitting of each peak. This does not account for other sources of uncertainty, for example the extrapolation of fits of the elastic constants used to calculate S . The three data sets have three different trends. Run A has low values over its entire range, even becoming negative at higher pressure. For run B there is a peak in αt near 100 GPa. This may correspond to a deformation of the cell or gasket, as such a process is known to happen in the intermediate range of the loading curve, and the difference from Run A could be the use of beveled anvils [24]. Overall for both runs values are quite low, indicating good hydrostatic conditions.

Run C displays more variable behavior and higher absolute values, though like with the other data they are still less than 1% of the total pressure (Ref. [19], Fig. S2). The larger spread in values can be linked to the reduced area covered by the detector (compare the two panels on the right-hand side of Fig. 1), making it harder to view complete rings on the detector that are necessary to precisely evaluate differential stress. It may also be due to challenges associated with the smaller culet size and the inevitable differences in preparation of each experiment. A negative αt would correspond to the radial stress on the sample being larger than the axial stress, which is hard to reconcile with the fact that pressure is applied axially. While this is also the case with Run A, for that experiment

positive values are within the error and the overall conclusion is that αt is too small to be reliably measured.

We note that t is linearly related to the shear strength of the material. The high compressibility of Bi means it is unable to support a large deviatoric stress, keeping t low. This is part of what makes it a good pressure calibrant and was part of the argument used elsewhere for why Bi itself could serve as a pressure medium. However, our results for the first two runs are a little lower than those of other studies that did not use a soft PTM [15,22], where t values of around 0.5 GPa were seen by 200 GPa, though this is again hampered by the large relative uncertainty. We attribute the difference to the use of the soft Ne pressure medium, which is even more malleable than Bi and thus even better able to redistribute the applied stress, a conclusion backed up by the comparison of $P(V)$ data.

VI. SUMMARY

Our data show that by 260 GPa the volume of Bi is about 45% of its estimated ambient pressure value. This can be compared to values for some common pressure markers: 70%, 63%, 58%, and 40% for Pt, Au, Cu, and NaCl (B2, CsCl-type phase), respectively [16,25]. Bismuth has a larger change in volume than the three coinage metals, which is especially beneficial to experimental precision at higher pressure, where $V(P)$ flattens out. While not quite as compressible as NaCl, Bi has a much higher density and molar mass, leading to a

stronger XRD signal. At high pressure, once it is fully in the bcc phase, Bi thus has advantages over typical calibrants.

In three different experiments, we have seen consistent behavior of the volume of the bcc Bi-V phase up to 260 GPa. These data show good overlap and can be readily fit to a Vinet equation of state. The upward deviation of previous $P(V)$ data over 200 GPa and the conclusions of lineshift analysis show that Ne better reduces anisotropic stress than Bi alone. As seen in Fig. 3, at relatively low pressure the difference is minor. But when extending to the highest measured pressures or considering experiments beyond this range, the differences become significant. The information provided here can help motivate interest in Bi as a pressure calibrant above 10 GPa in XRD experiments. It also makes clear that the use of the softest pressure medium possible is necessary to reduce deviatoric stress and obtain accurate equations of state.

ACKNOWLEDGMENTS

This work was performed under the auspices of the U.S. Department of Energy by Lawrence Livermore National Laboratory under Contract No. DE-AC52-07NA27344. Portions of this work were performed at HPCAT (Sector 16), Advanced Photon Source (APS), Argonne National Laboratory. HPCAT operations are supported by DOE-NNSA's Office of Experimental Sciences. The Advanced Photon Source is a U.S. Department of Energy (DOE), Office of Science User Facility operated for the DOE Office of Science by Argonne National Laboratory under Contract No. DE-AC02-06CH11357.

-
- [1] M. I. McMahon, O. Degtyareva, and R. J. Nelmes, *Phys. Rev. Lett.* **85**, 4896 (2000).
- [2] O. Degtyareva, M. McMahon, and R. Nelmes, *High Pressure Res.* **24**, 319 (2004).
- [3] R. J. Husband, E. F. O'Bannon, H.-P. Liermann, M. J. Lipp, A. S. Méndez, Z. Konôpková, E. E. McBride, W. J. Evans, and Z. Jenei, *Sci. Rep.* **11**, 14859 (2021).
- [4] Y. Akahama, H. Kawamura, and A. K. Singh, *J. Appl. Phys.* **92**, 5892 (2002).
- [5] J. Hu, K. Ichianagi, T. Doki, A. Goto, T. Eda, K. Norimatsu, S. Harada, D. Horiuchi, Y. Kabasawa, S. Hayashi *et al.*, *Appl. Phys. Lett.* **103**, 161904 (2013).
- [6] M. G. Gorman, A. L. Coleman, R. Briggs, R. S. McWilliams, D. McGonegle, C. A. Bolme, A. E. Gleason, E. Galtier, H. J. Lee, E. Granados *et al.*, *Sci. Rep.* **8**, 16927 (2018).
- [7] C. M. Pépin, A. Sollier, A. Marizy, F. Occelli, M. Sander, R. Torchio, and P. Loubeyre, *Phys. Rev. B* **100**, 060101(R) (2019).
- [8] M. G. Gorman, R. Briggs, E. E. McBride, A. Higginbotham, B. Arnold, J. H. Eggert, D. E. Fratanduono, E. Galtier, A. E. Lazicki, H. J. Lee *et al.*, *Phys. Rev. Lett.* **115**, 095701 (2015).
- [9] J. Wills, O. Eriksson, P. Andersson, A. Delin, O. Grechnev, and M. Alouani, *Full-Potential Electronic Structure Method*, Springer Series in Solid-State Sciences Vol. 167 (Springer, Berlin, 2010).
- [10] P. Söderlind and D. Young, *Computation* **6**, 13 (2018).
- [11] L. Nordström, J. M. Wills, P. H. Andersson, P. Söderlind, and O. Eriksson, *Phys. Rev. B* **63**, 035103 (2000).
- [12] B. Sadigh, A. Kutepov, A. Landa, and P. Söderlind, *Appl. Sci.* **9**, 5020 (2019).
- [13] D. Alfè, *Comput. Phys. Commun.* **180**, 2622 (2009).
- [14] P. Söderlind, B. Grabowski, L. Yang, A. Landa, T. Björkman, P. Souvatzis, and O. Eriksson, *Phys. Rev. B* **85**, 060301(R) (2012).
- [15] L. Liu, H. X. Song, H. Y. Geng, Y. Bi, J.-a. Xu, X. Li, Y. Li, and J. Liu, *Phys. Status Solidi B* **250**, 1398 (2013).
- [16] A. Dewaele, P. Loubeyre, and M. Mezouar, *Phys. Rev. B* **70**, 094112 (2004).
- [17] A. Dewaele, F. Datchi, P. Loubeyre, and M. Mezouar, *Phys. Rev. B* **77**, 094106 (2008).
- [18] Y. Fei, A. Ricolleau, M. Frank, K. Mibe, G. Shen, and V. Prakapenka, *Proc. Natl. Acad. Sci. USA* **104**, 9182 (2007).
- [19] See Supplemental Material at <http://link.aps.org/supplemental/10.1103/PhysRevB.107.224104> for additional data and experimental details, which includes Refs. [3,16–18].
- [20] A. K. Singh, C. Balasingh, H.-k. Mao, R. J. Hemley, and J. Shu, *J. Appl. Phys.* **83**, 7567 (1998).
- [21] A. K. Singh and T. Kenichi, *J. Appl. Phys.* **90**, 3269 (2001).
- [22] A. Singh, E. Menéndez-Proupin, G. Gutiérrez, Y. Akahama, and H. Kawamura, *J. Phys. Chem. Solids* **67**, 2192 (2006).
- [23] G. Gutiérrez, E. Menéndez-Proupin, and A. K. Singh, *J. Appl. Phys.* **99**, 103504 (2006).
- [24] B. Li, C. Ji, W. Yang, J. Wang, K. Yang, R. Xu, W. Liu, Z. Cai, J. Chen, and H.-K. Mao, *Proc. Natl. Acad. Sci. USA* **115**, 1713 (2018).
- [25] S. M. Dorfman, V. B. Prakapenka, Y. Meng, and T. S. Duffy, *J. Geophys. Res.: Solid Earth* **117**, B0821 (2012).